Low friction and wear resistant coatings

Carvalho, Nuno Jorge Marcolino

2

DESCRIPTION OF THE METHODOLOGY

2.1 INTRODUCTION

Mechanical components and metal cutting tools are currently facing higher performance requirements. The use of surface coatings opens up the possibility for a material design in which the specific properties are located where they are mostly needed. However, the ability of the coating to protect the substrate and enhance the mechanical and tribological properties of the composite system relies mainly on the deposition process, morphology, elemental composition, and microstructure. In this chapter, the deposition processes and methods utilised for coating characterisation as well as the equipment used are presented and discussed. Further, the techniques employed for mechanical and tribological evaluation, namely, nanoindentation and rolling contact fatigue are considered.

Equation Section 2

2.2 DEPOSITION TECHNIQUES

The coatings used in this thesis were supplied by Balzers Ltd. Therefore, only the most important features of each process will be summarized. Physical vapour deposition (PVD) techniques are atomistic deposition processes which operate at relatively low temperatures. The deposition process of wear protective coatings can be described as follows. Before insertion into the chamber, the substrate is degreased and dried with N_2 gas. Then the coating

chamber is evacuated to a high vacuum, and by heating at a temperature of approximately 450 °C, a high current density plasma beam is used to de-gas the surface. The chamber is set at a pressure, depending on the process, in a range of $1.3x10^{-2}$ to 1.3 Pa (10^{-4} – 10^{-2} Torr) while cleaning of the substrate is performed by sputtering. The next step consists of atomisation or vaporisation of material from a solid source and deposition on the substrate to form the coating. Since the coating is created from a flux of atoms approaching the substrate with a limited range of directions, the microstructure has a columnar nature.

There are several ways in which a coating can be produced by PVD, but recent techniques all include the plasma assisted PVD processes (PAPVD). The basic PAPVD is commonly entitled ion plating. It consists of bombarding the substrate surface, considered as the negative electrode in a glowing discharge of argon, with a flux of high energy ions sufficient to cause appreciably sputter-cleaning of the surface before and during film formation. Moreover, the coating material is ionised in the plasma by collision and electron impact reactions and accelerated in the electric field of biased substrates so that condensation and coating formation take place under the influence of ion bombardment. Consequently, PAPVD provides coatings that are very dense. The coatings contain only few macroscopic defects and possess a very good adhesion to the substrate.[1,2] A large proliferation of techniques, although all based on the principles of mass transfer from one source to a substrate, has enabled deposition of alloy compounds and multilayer compositions. However, they all include the ion plating technology and can be divided into two main groups: evaporation PVD and sputtering PVD.

In evaporation PVD technology, the coating material is placed in a crucible and heated under vacuum to a liquid phase or sublimation point. Currently, there are four main methods for evaporation: resistance heating, induction heating, arc and electron beam gun (e-gun) sources.[3] TiN studied in this thesis was deposited in a BAI 640R coating unit using the electron beam gun source. The unit is schematically shown in figure 2.1a. Pure Ti was evaporated from a crucible with a high voltage electron beam by means of a 270° electron gun, in the presence of a certain pressure of nitrogen. The e-gun produced electrons by a hot filament (made of tungsten), which were accelerated by an electrical field located between the anode and the filament (cathode) to form the beam. The

270° deflection into the crucible was achieved by a magnetic coil. A major advantage of the 270° e-gun is the possibility to create a desired beam shape by varying the electrical current passing through the magnet coil, thereby melting the material evenly. In addition, there is effectively no limit with respect to the melting point of materials that can be evaporated. A plasma beam was operated between the hot filament and the crucible so as to ionise the metal vapour, the nitrogen, and the argon gas. The vaporised titanium atoms reacted with the ionised nitrogen creating the TiN compound which was subsequently deposited on the substrate. The substrate was at temperature of 480 °C during the deposition process.

Sputtering is an atomistic process that uses a glowing discharge to generate a flux of ions (Ar^+) incident on the target surface. These ions cause atoms, and occasionally cluster of atoms to be ejected from the target surface through the transfer of momentum. A schematic image of the coating unit BAI 830, used to deposit the WC/C coating is shown in figure 2.1b. The application of magnetrons, in this case operating in a DC mode, adds a magnetic field to the electric field. In this way the electrons are kept in trajectories close to the target surface, increasing the number of ionising collisions of electrons with argon and therefore enhancing the sputter and deposition rates.[4]

The confinement of the plasma is done by the rectangular planar magnetron, consisting of three rows of permanent magnets with alternating polarity arranged behind the target, generating a closed endless tunnel of magnetic field lines. With this arrangement, the whole vacuum coating chamber can be used as the anode, or alternatively an anode of metal rods is positioned near the cathode of the planar magnetron. This unit has six rectangular planar magnetrons arranged in a circle, with the substrates passing consecutively as they perform planetary rotation. One chromium target, for the deposition of an initial interlayer, and five WC targets for the remaining coating were used.

The carbon phase of the WC/C coating was grown from a plasma containing hydrocarbon (acetylene, C_2H_2) as the reactive gas. The deposition procedure consisted of initially depositing an interlayer of chromium to promote coating adhesion and subsequently depositing the WC/C multilayers, i.e. DC magnetron sputtering of the WC targets commenced and acetylene was

introduced into the chamber. The thickness of the multilayers was controlled by the rotation speed imposed to the substrate holder. The substrate temperature was kept about 200 - 250 °C during coating deposition.

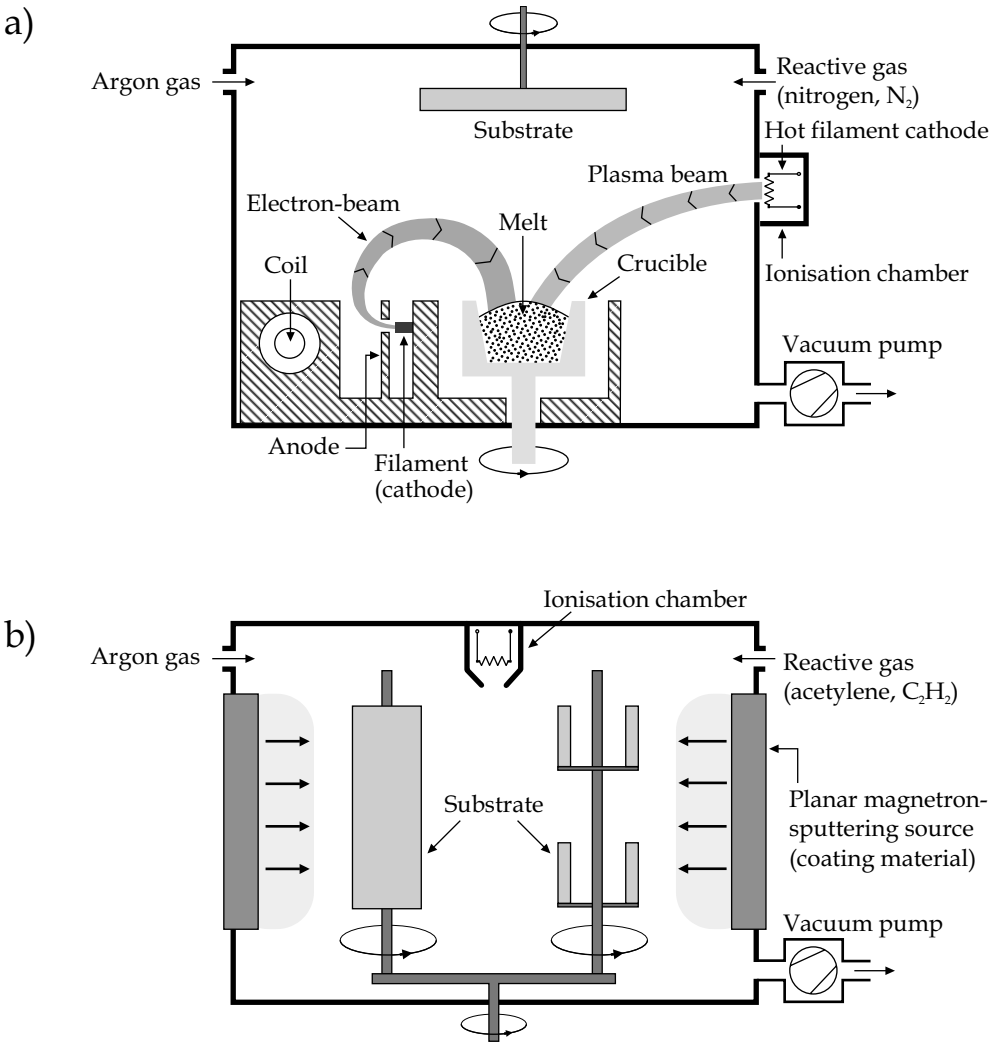

Figure 2.1 *(caption on facing page)*

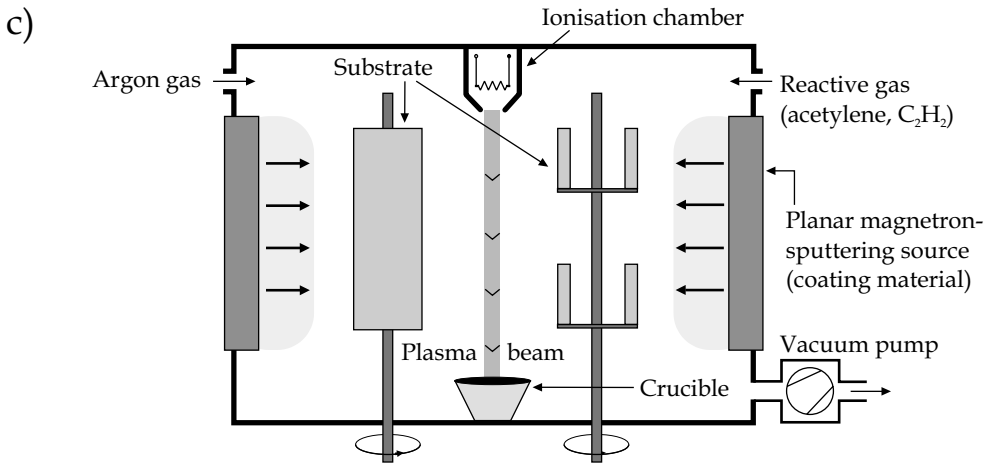

Figure 2.1 *Schematic view of the* (a) *evaporation unit where the TiN was deposited,* (b) *sputtering unit used for the WC/C multilayers deposition, and* (c) *hybrid unit employed to deposit the TiN/(Ti,Al)N multilayers. The TiN layer was cathodic arc-evaporated while the (Ti,Al)N layer was magnetron sputtered.*

The TiN/(Ti,Al)N multilayers were deposited in a BAI 830 coating unit. However, in this case, using a hybrid process which combined reactive arc evaporation of pure Ti - from a crucible with a thermionic arc source to deposit TiN - and reactive magnetron sputtering of a titanium-aluminium alloy target for deposition of the (Ti,Al)N compound. A schematic of the modified coating unit is shown in figure 2.1c. The cathodic arc process uses a glowing discharge plasma between the cathode and the crucible. The principal merit of arc evaporation is that no molten pool is formed, allowing the crucibles to be fitted in any orientation. Further, a major part of the emitted source material becomes highly ionised as it passes through the arc.[5]

Nevertheless, a disadvantage of arc-evaporation is the fact that it also produces macroparticles in the coating matrix. They are created by droplets of a metal ejected from the source surface as the arc locally and rapidly melts the source material.[6] The (Ti,Al)N layers were produced by magnetron sputtering of stoichiometric Ti-Al target materials, using a similar process as for the WC layers described above, in an argon and nitrogen atmosphere. However, the substrate temperature was the same as for the deposition of TiN coatings.

2.3 METHODS OF CHARACTERISATION

To understand the structure-property relationship of coated components and ultimately be able to predict their tribological behaviour, it is imperative to gather as much information on morphology, elemental and phase composition and microstructure as possible. Table 2.1 summarises the characterisation techniques utilised in this thesis.

Table 2.1 *Analysis techniques utilised to evaluate coating morphology, composition, and microstructure.*

Coating property	Technique
Morphology, thickness	Scanning electron microscopy (SEM)
Surface topography	Scanning confocal microscopy (SCM)
Phase composition, texture	X-ray diffraction (XRD)
Elemental composition	Auger electron spectroscopy (AES), energy dispersive x-ray spectrometry (EDS), electron energy-loss spectroscopy (EELS)
Microstructure	Transmission electron microscopy (TEM), high resolution transmission electron microscopy (HRTEM), energy filtering transmission electron microscopy (EFTEM)

2.3.1 MORPHOLOGY

Scanning electron microscopy (SEM) is an invaluable tool to get a general picture of the coating morphology. Additionally to plan-view, fractured cross-sections of coated samples were regularly studied as they often allow for a straightforward observation of the coating morphology (size and shape of the

columns), cohesion and adhesion to the substrate. In this thesis, scanning electron microscopy was performed by a Philips XL30-FEG SEM and a Philips XL30S-FEG SEM, both equipped with a field emission gun.

2.3.2 SURFACE TOPOGRAPHY

A quantitative complimentary method to examine the surface morphology is obtained by analysing the surface roughness using surface profilometry. The surface roughness, R_a - value, of the coated samples was measured using a Mitotoyo Surftest 500 profilometer, whereas the topography was investigated by a Nanofocus μSurf confocal scanning optical microscope with a white light source.

2.3.3 PHASE COMPOSITION

X-ray diffraction (XRD) is widely utilised for phase determination and structural (texture, defects) analysis of films. Nevertheless, the observed diffraction peaks are often quite broad due to small grain sizes and high defect concentrations. Consequently, the precision of lattice constant determinations is generally not better than 0.01 Å.[7] However, 0.01 Å accuracy is often sufficient for general phase identification. Thus, this technique was utilised to identify the phases present in the films. The degree of preferred orientation of the coatings was determined by calculation of a texture coefficient, T_c, defined as:[8]

$$T_c = \frac{I_{(hkl)} / I_{0\,(hkl)}}{\frac{1}{n}\sum_{1}^{n}\left(I_{(hkl)} / I_{0\,(hkl)}\right)} \qquad (2.1)$$

where $I_{(hkl)}$ is the intensity of the reflection from the (hkl) plane, $I_{0\,(hkl)}$ is the intensity from the same plane in a standard reference sample, and n is the number of reflections considered. Thus, a T_c value of 1 means a randomly oriented coating, whilst for values greater than 1, the plane is considered to have a preferred orientation. The XRD measurements were carried out using a Philips PW1710 based diffractometer with Cu-Kα radiation in $\theta/2\theta$ mode and generator settings of 40 kV and 30 mA.

2.3.4 CHEMICAL COMPOSITION

Analysis of elemental composition was performed by several techniques. Compositional Auger electron spectroscopy (AES) line profiles were performed on samples prepared in a similar way as the cross-sectional TEM specimens, described in detail below. This procedure enables the area of interest to be evenly smooth and free of contaminants. Prior to Auger data collection the samples were Ar^+ ion sputtered to remove any possible remaining oxide layer. In order to get the intensity in the direct AES spectra approximately quantitative, the Auger signal was obtained using the function $(N_1 - N_2)/(N_1 + N_2)$ where N_1 is the signal on an Auger electron peak and N_2 is that on the background at slightly higher energy. This function has an excellent signal-to-noise behaviour and largely removes topographical effects that might be present in line profiles.[9] The equipment used was a JEOL JAMP 7800F, a combined UHV-Scanning–Auger/electron microscope (SEM/SAM) system equipped with a hemispherical analyser (HAS). Typically, the electron beam current was 2.2 nA at 10 kV accelerating voltage, generated by a field emission gun (FEG). These conditions yield a beam spot size of ~15 nm, allowing a lateral resolution down to nanometer length scales.

Analytical transmission electron microscopy was carried out using a JEOL 2010 FEG, operating at 200 kV, equipped with an EDAX energy dispersive analyser and a post-column Gatan Imaging Filter (GIF). Energy dispersive x-ray spectroscopy (EDS) analyses were performed by line profile in cross-sectional TEM specimens using an optimum nominal probe size of 0.5 nm FWHM. The distance between points was varied depending on the layer thickness. The post-column GIF was used for elemental mapping utilising the three window technique, which consists of acquiring one post-edge and two pre-edge images. This technique was employed in order to extract the characteristic signal superimposed on the background, estimated from the two pre-edge images and subtracted from the post-edge image. The procedure enables maps of edge intensity versus position in the film, i.e. an independent recording of the concentration profile.

2.3.5 MICROSTRUCTURE

The coating microstructure, e.g. grain size, phase and lamella thickness, was studied from plan-view and cross-sectional specimens by conventional and high resolution transmission electron microscopy. The observations were carried out using the following microscopes: JEOL 4000 EX/II operating at 400 kV and JEOL 2010 FEG operating at 200 kV. The electron-optical parameters of the microscopes are given in table 2.2.

Table 2.2 *Properties of the transmission electron microscopes used for microstructural analyses.*

	JEOL 4000EX/II	JEOL 2010F
Emission	LaB_6 filament	Field emission gun
Operating voltage (kV)	400	200
Spherical aberration coefficient (mm)	0.97	~1.00
Spread of focus (nm)	7.8	4.0
Beam convergence angle (mrad)	0.8	0.1
Information limit resolution (nm)	0.14	0.11
Point resolution (nm)	0.17	0.23
Optimum defocus (nm)	-48.9	-61.0

CHAPTER 2

SPECIMEN PREPARATION FOR TEM

There are several techniques described in literature for the preparation of plan-view and cross-sectional TEM specimens.[10,11] In this thesis, specimen preparation for plan-view TEM consisted of cutting out a disc from the region of interest with 3 mm diameter using the Nd-YAG laser, followed by grinding and polishing from the substrate side to a thickness of 50 μm. The disc was further thinned to electron transparency by dual gun Ar^+ ion milling. The specimen was kept on rotation while the Ar^+ beam at 5kV with an ion current of 0.5 mA was directed towards the substrate side with an incident angle of 8° from the specimen surface. Final etching was performed briefly from both sides with the tilt angle reduced to 4° in order to clean the coating surface, to reduce ion induced artefacts and to remove any amorphous redeposited surface layer.

For cross-sectional TEM specimen preparation of heterogeneous materials, however, only a few methods exist in literature which minimises the differential thinning that occurs on either side of the interface of interest. The method used is a refinement of the one developed by *Barna*,[11] which is particularly advantageous when low angle thinning is required. The basic tool is a titanium disc (diameter 3 mm, thickness 0.3 mm) containing three slots made by a Nd-YAG laser. The width of the central rectangular slot is 800 μm and should be chosen so as to be slightly larger than the thickness of the two pieces being embedded.

The steps involved in preparation are illustrated in figure 2.2 and were as follows. After cutting, the two small pieces were placed film-to-film in the central slot (figure 2.2a). The walls of the slot were then bent using a small rounded screwdriver until the samples touch each other (figure 2.2b). The edges of the side slots were cut using a small chisel causing a displacement at the ends of the walls of the central slot (figure 2.2c). The walls, acting like small springs, fixed the two pieces. The sample was then embedded in a two component glue (Gatan glue). As a result of capillary force and gravity, the bonding material penetrated all the slots and filled them, appearing at the top of the Ti disc (figure 2.2d). The specimen was then placed in a temperature-controlled oven to solidify the glue. To avoid bonding between the hotplate and the specimen, a small piece of aluminium foil was placed underneath. After solidification, the

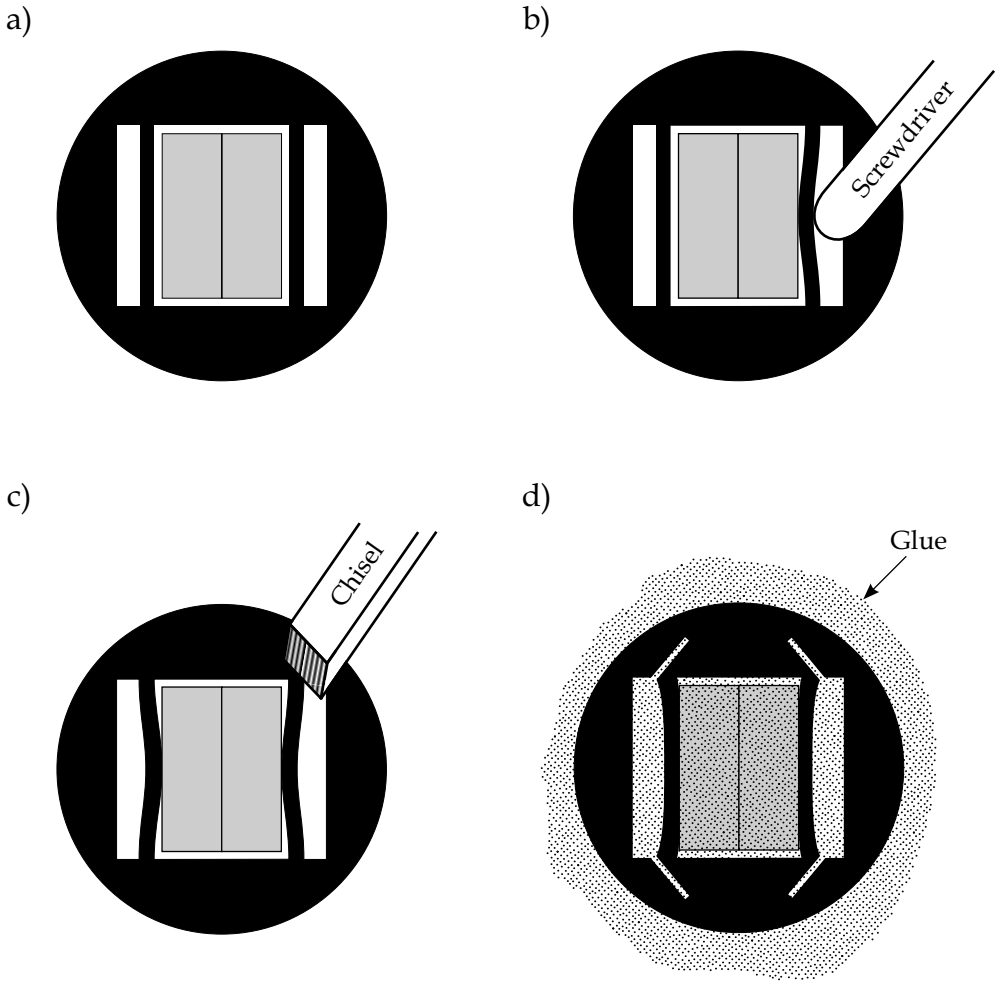

Figure 2.2 *Steps involved in the preparation of a cross-sectional TEM specimen for low angle ion milling. The 3 mm diameter titanium disc is shown in black. The two grey rectangles represent the sample:* (a) *Two slabs of coated material approximately 1300x350x300 m are placed edge-on, film-to-film in the large rectangular slot of the titanium grid;* (b) *a small rounded tool is inserted into each side rectangular slots and twisted to deform the thin band of titanium between the central and side slots. This holds the two pieces together with the coatings in the centre of the sample;* (c) *a small chisel is pressed into the titanium grid, at the positions shown, to bend further the thin bands, and thus improve the grid support of the samples;* (d) *The grid containing the samples is immersed in a drop of Gatan glue, and placed in an oven to cure the glue.*

bonding material together with the aluminium foil was cut away from the titanium disc along its perimeter, which was followed by mechanical grinding and polishing (using a Tripod Polisher) on both sides to a thickness of 50 μm. This technique obviously has an advantage in the preparation of brittle materials due to the supporting titanium disc, without the disadvantage of the occurrence of shadowing during low angle ion beam thinning. Ion beam milling was performed on the mechanically ground and polished specimen with two guns in mirror-image position on both sides, using a Gatan PIPS, model 691. The angle of incidence was 6° (ion energy 4 kV and ion current 40 μA) and the specimen was rotated. Final thinning to electron transparency was accomplished by rocking the specimen ±30° perpendicular to the coating-substrate interface with an incoming ion beam at 4°. This process continued until perforation took place and the hole reached the region of interest. Finally, the surface contaminants (due to redeposited material) were reduced by using an ion energy of 2 kV and ion current of 4 μA while rotating the specimen.

In order to investigate the coated system response beneath the trigonal impression of a nanoindentation, cross-sectional TEM specimens from the contact sites were prepared. The novel method makes use of the titanium disc described above. Two thin slabs (1300x50x350 μm) of coated material with the coating on the 1300x50 μm surface were fitted in the 100 μm central slot. Then three rows of indentations, distributed over the coated surface, were performed in each sample with a load ranging from 50 mN to 400mN. After performing the indentations, the slabs were removed from the grid and fitted film-to-film in a 700 μm slot of other grid followed by embedding in a two component glue. When the glue was cured, which was accomplished by placing the specimen in a temperature-controlled oven, it was polished (using a Tripod Polisher) to remove 10 μm of material from each side. The following ion beam milling process was similar to the one employed for preparation of cross-sectional TEM specimens. However, to control the thinning process and to ensure that the electron transparent area was in the contact sites, the ion milling was periodically stopped and the specimen was examined with scanning electron microscopy.

2.4 EXPERIMENTAL METHODS

2.4.1 MICROINDENTATION

The first microhardness tester was developed in 1925 by *Smith* and *Sandland*.[12] They designed a square-based diamond pyramid indenter with a face angle of 136°, whose geometry gave hardness numbers values identical to the Brinell numbers using a hardened steel ball. This fact made the Vickers hardness test widely accepted and very easy to implement. The Vickers hardness number, H_V, is obtained as the ratio of the applied load to the area of the resulting indentation. With the given pyramid geometry the hardness is expressed by

$$H_V = 2\sin\left(\frac{\theta}{2}\right)\frac{P}{d^2} \tag{2.2}$$

where θ is the angle between opposite faces of the diamond, P is the applied load in kgf, and d is the indentation diagonal in mm. It should be noted that the indentation depth D is close to one-seventh of the diagonal. The influence of the load on the Vickers hardness value is not explicit in this relation, but it can be seen by the *Bückle*[13] representation of the hardness evolution in relation to the load in figure 2.3. This representation shows that the measured hardness value is largely dependent on the load range. Therefore, every hardness measurement should indicate which load was applied. In order to account for the hardness-load dependence, several models[14-16] have been proposed for both bulk materials and coated samples.

2.4.2 NANOINDENTATION

In the past two decades, a great deal of effort has been directed towards the development of techniques for characterising the mechanical properties of thin films and small volumes of material. Load and depth sensing indentation, commonly referred to as nanoindentation, is a way by which this has been achieved.[17-19] However, the material properties that can be probed with this technique depends on the indenter tip geometry. In general, sharp, geometrically-similar indenters such as the Berkovich triangular pyramid are

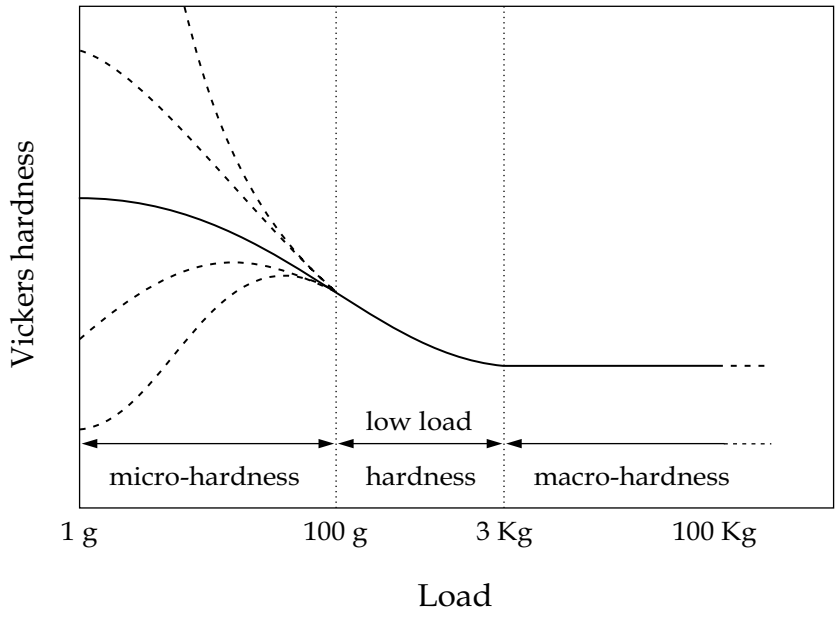

Figure 2.3 *Schematic representation of hardness versus load. In the range of very low loads the results are susceptible to unusually high discrepancies as depicted by the dashed lines, which are hypothesised results of many different observers. The range of medium loads yields reproducible but load-dependent hardness values, while at high loads the hardness values are constant, after Bückle.*[13]

useful when one wishes to probe properties at the smallest possible scale. This tip is often preferred over the Vickers for hardness measurements because the apex can be more readily fashioned to meet at a point rather than the inevitable line that occurs with the Vickers four-sided geometry. Moreover, it has no major flaws and is easier to calibrate. Therefore, the force/area relationship can be reliably calculated at very low loads.

The properties routinely measured with the Berkovich indenter are the hardness and the elastic modulus,[20] and although less well developed, methods are also available for measuring strain rate sensitivity, and internal friction.[21] When the specimen temperature can be controlled, it is also possible to determine parameters characteristic of thermally-activated plastic flow, such as the activation energy and stress exponent for creep.[22]

With Vickers or cube cornered indenter tips, it is possible to make indentations in brittle materials at a load high enough to produce radial cracks extending from the edges of the contact. This method allows one to explore the fracture toughness and the state of surface stresses at the sub-micron scale in small volumes of material.[23,24] However, in some cases the Vickers indenter is not suitable for assessing the fracture toughness. As *Vepřek et. al.*[25] have shown for superhard nanocomposites, due of their high elasticity and high toughness, only circular cracks within the crater but no radial ones are formed, even when the indentation depth is larger than the coating thickness.

Spherical indenters are also commonly employed by ultra-low load indentation methods.[26,27] The major benefit of the spherical indenter is that the indentation contact is homogeneous and starts elastically, and then changes to elastic/plastic at higher loads, thereby permitting one to investigate yielding and associated phenomena. However, in some situations it is difficult to identify experimentally the initial yielding because the onset of plasticity is well below the surface.[28] Using this technique, in principle, it is also possible to determine mechanical properties such as the elastic modulus, yield stress, and the strain-hardening behaviour of a material. The foremost drawback of spherical indenters is the difficulty to obtain precise spherical geometries with radius less than about 50 micron in hard materials like diamond. Since most methods assume the perfect spherical geometry, this leads in some cases to a large inaccuracy.[29]

MODEL TO EXTRACT HARDNESS AND ELASTIC MODULUS

In order to determine the hardness and elastic properties of a material using load and depth sensing indentation techniques, several methods have been developed.[20,30-32] One of the important advantages of these methods is that it is not necessary to measure the area of the hardness impression by imaging, thereby facilitating property measurements at the sub-micron scale. The contact area and the mechanical properties are determined from the data of one complete cycle of loading and unloading. The unloading data is treated assuming that the displacement recovered is largely elastic. Then, the hardness

and Young's modulus can be determined by solving the elastic contact problem.[33]

The mathematical foundations for the contact problem of indentation of an elastic half-space by a rigid punch were considered more than a century ago by *Boussinesq*[34] and *Hertz*[35]. *Boussinesq* published a solution for the problem of contact of an elastic body loaded by a rigid, axisymmetric indenter. Later, *Love* used his method to derive solutions for cylindrical[36] and conical[37] punches. On the other hand, *Hertz* developed a method for analysing the elastic contact between two spherical surfaces with different radii and elastic constants. His solutions are the skeleton of the field of contact mechanics and provide a way by which the effects of non-rigid indenters can be included in the analysis. However, a solution for the contact problem was only derived in 1945 by *Sneddon*[38], who established an analytical procedure for obtaining the relationships of load, displacement, and contact area for a punch of arbitrary axisymmetric shape. His results show that the load-displacement relationships for simple punch geometries can be expressed as

$$P = \alpha h^m \tag{2.3}$$

where P is the indenter load, h is the total elastic displacement of the indenter, m is 1, 1.5, and 2 for a flat cylindrical punch, parabola of rotation, and cone, respectively, and α is a constant. *Stillwell* and *Tabor*[30] performed the earliest experiments in which load and displacement sensing indentations by conical indenters were used to measure mechanical properties. Their experiments revealed that upon unloading the shape of the hardness impression was still conical, and only the depth had recovered, resulting in a larger included tip angle. Therefore, the elastic contact solutions could be applied and the plasticity accounted, by taking into consideration the shape of the deformed surface. With these results, they demonstrated that the elastic modulus and the size of the contact impression could be derived accurately from the shape of the unloading curve and the total amount of recovered displacement.

Another key development was the definition of reduced modulus, which includes the effects of non-rigid indenters on the load-displacement behaviour, via the equation

$$\frac{1}{E_r} = \frac{(1-\nu^2)}{E} + \frac{(1-\nu_i^2)}{E_i} \tag{2.4}$$

where E and ν are the Young's modulus and Poisson's ratio, respectively, for the specimen and E_i and ν_i the corresponding quantities of the indenter. The first experiments to obtain load-displacement data which could be used to measure the elastic modulus, were done by *Bulychev* and co-workers[39] using a microhardness testing apparatus. They analysed the data according to the equation

$$S = \frac{dP}{dh} = \frac{2}{\sqrt{\pi}} E_r \sqrt{A} \tag{2.5}$$

where S is the stiffness in the contact between the indenter and the specimen, i.e. the slope of the upper portion of the unloading data, and A is the projected area of the elastic contact measured from the indentation hardness impression. Eq. (2.5) has its origins in the elastic contact theory[40]. Although it was originally derived for a conical indenter, *Bulychev et al.* showed that the equation could be applied for spherical and cylindrical indenters. Subsequently, *Pharr et al.*[33] showed that Eq. (2.5) applies to any indenter that can be described as a body of revolution of a smooth function. Moreover, *King*,[41] using a finite element method, showed that when Eq. (2.5) is rewritten as

$$S = \frac{2}{\sqrt{\pi}} \beta E_r \sqrt{A} \tag{2.6}$$

it can be applied to indenter geometries which are not described as bodies of revolution, like flat-ended punches with square (Vickers-like) and triangular (Berkovich-like) cross sections, providing β is taken to be 1.012 and 1.034, respectively.

In the late 1980's *Doerner* and *Nix*[32] presented a method to determine the hardness and modulus from load-displacement data using Eq. (2.5). They recognized that for most metals, during initial unloading the area in contact

with the indenter remains constant. Accordingly, the elastic behaviour could be modelled as that of a blunt punch indenting over the contact area of an elastic solid. To evaluate the contact area independently, they proposed to extrapolate the initial part of the unloading curve to zero load and determine the extrapolated depth. Then, using the indenter shape function, the contact area can be calculated. Knowing the contact area, the hardness, H, which is equivalent to the average pressure under the indenter, is calculated from

$$H = \frac{P^{max}}{A} \tag{2.7}$$

where P^{max} is the maximum load.
Today, there is an overall agreement that the unloading curve typically deviates from a straight line, especially for hard ceramic materials such as Ti-based coatings. For these materials, the slope of the unloading curve and consequently, the projected area of the elastic contact decrease continuously during unloading due to elastic recovery within the indentation.

Oliver and *Pharr*[20] have developed a procedure that accounts for the elastic recovery by expanding the assumptions developed by *Loubet et al*.[31] and *Doerner* and *Nix*,[32] without assuming a flat punch geometry. The method expresses the load-displacement relation derived by *Sneddon*,[38] Eq. (2.3), for purely elastic material the more general form by

$$P = \alpha(h - h_f)^m \tag{2.8}$$

where the total displacement is now modified for the indenter impression, being h_f the final displacement after complete unloading, as shown schematically in figure 2.4, and α, m are constants. A drawback of the analysis proposed by *Oliver* and *Pharr* is that the suggested power law relationship does not take into account any residual plasticity present in an elastic/plastic material. Their analysis procedure begins by rewriting Eq. (2.6) as

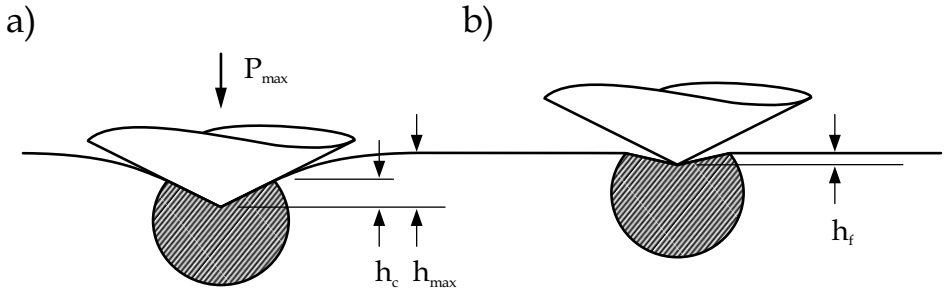

Figure 2.4 *Schematic representation of the deformation during nanoindentation:* (a) *indenter tip is pressed into the material at maximum load;* (b) *unloading state with decreased contact area. The hatched area represents plastically deformed material.*

$$E_r = \frac{1}{\beta}\frac{\sqrt{\pi}}{2}\frac{S}{\sqrt{A}} \tag{2.9}$$

which relates the reduced modulus, E_r, to the contact area, A, and the measured stiffness, S. Then, the unloading curve is fitted to the power-law relation of Eq. (2.8), where α, m and h_f are empirically determined fitting parameters. The unloading stiffness is subsequently obtained by differentiating the load-displacement relation at the maximum depth of indentation, $h = h_{max}$, leading to:

$$S = \frac{dP}{dh}(h = h_{max}) = m\alpha(h_{max} - h_f)^{m-1} \tag{2.10}$$

The depth along which contact is made between the indenter and the specimen, called contact depth, h_c, is also estimated from the load-displacement data through

$$h_c = h_{max} - \varepsilon\frac{P_{max}}{S} \tag{2.11}$$

it depends on the indenter geometry, being $\varepsilon = 0.72$ for a conical indenter, $\varepsilon = 0.75$ for the Berkovich tip and $\varepsilon = 1$ for a flat punch. Figure 2.5 depicts the

cross section of an indentation and a schematic load-displacement curve, where all the parameters used in the analysis are identified. The indenter area function, A, is calculated using the unloading curve and based on the assumption that the elastic modulus is independent of the indentation depth, and the compliance of the specimen, C_S, and additional machine compliance, C_f, can be modelled as a two springs system in series. Taking the specimen compliance during elastic contact as the inverse of the contact stiffness, the contact area can be described by rewriting Eq. (2.5) as

$$A = \frac{\pi}{4}\frac{1}{E_r^2}\frac{1}{(C - C_f)^2} \tag{2.12}$$

where C is the total measured compliance, $(C = C_S + C_f)$.
The first estimate of the contact area is made for large indentations, by applying the indenter shape function for a perfect Berkovich indenter at the contact depth, which is given by

$$\begin{aligned} A(h_c) &= 3\sqrt{3}\, h_c^2 \tan^2\theta \\ &= 24.56\, h_c^2 \end{aligned} \tag{2.13}$$

where θ is the indenter included half-angle of 65.3°. Assuming that the large indentations are unaffected by tip rounding, the initial values of the elastic modulus and machine compliance are obtained by plotting C *vs* $A^{-1/2}$, where if the modulus is constant, the plot is linear and the intercept a direct measure of C_f. However, for real Berkovich indenters the shape function is far more complex due to tip rounding. Therefore, the contact area is now calculated for different indentation depths in a material with well-known, isotropic elastic properties (usually fused quartz), and plotted *vs* the corresponding contact depths. The resulting graph is fitted to a nine-term polynomial, and the new values of the machine compliance are then calculated by using the obtained area function and the procedure is repeated until convergence occurs and the indenter shape function is deduced. Then, the contact area can be determined from the load-displacement data, and the hardness and reduced modulus are calculated from Eq. (2.7) and Eq. (2.9), respectively.

a)

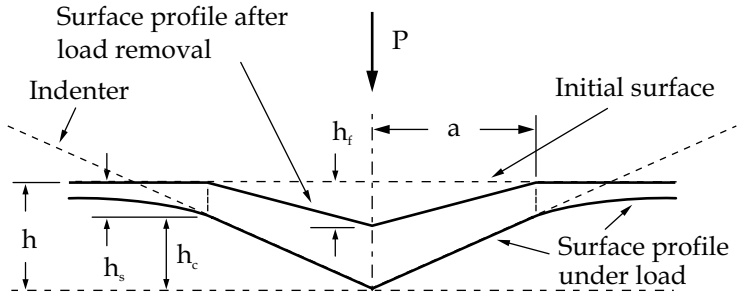

b)

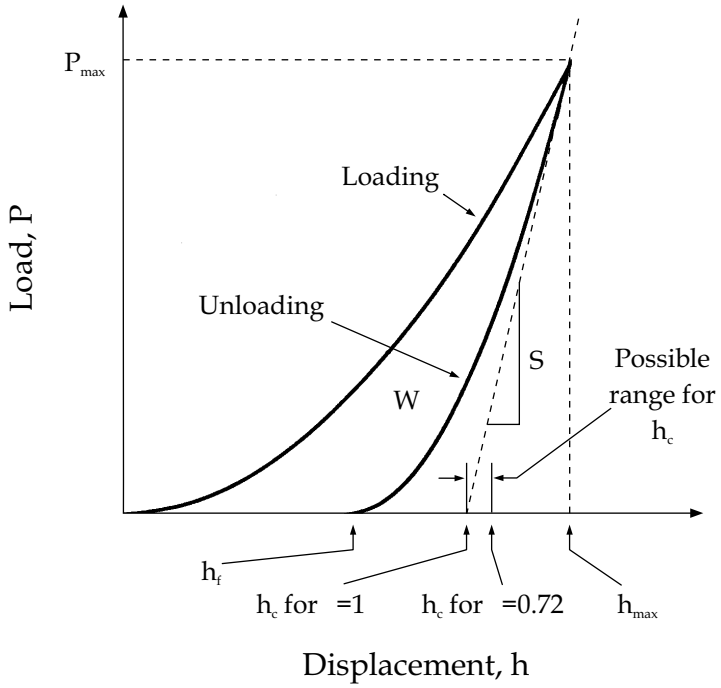

Figure 2.5 *Schematic representations of* (a) *a cross-section of an indentation and* (b) *the load versus indenter displacement showing the quantities used in the analysis as well as a graphical interpretation of the contact depth.*

INFLUENCE OF PILE-UP ON HARDNESS AND ELASTIC MODULUS

With a state-of-the art instrument and a careful analysis, the mechanical properties (i.e. hardness and elastic modulus) of several materials can be measured using this method with accuracies better than 10%.[20] There are, however, some materials in which the methodology can lead to a significant overestimate of the hardness and modulus due to an underestimate of the true contact area when large amount of pile-up forms around the residual impression. The underestimate of the contact area occurs because Eqs. (2.9) and (2.11) were derived from a purely elastic contact solution, and thus may not work well for elastic/plastic indentation. In the former situation, the material around the indenter always sinks-in, while in the latter the material may either sink-in or pile-up. Therefore, it is not surprising that the method has been found to work well for hard ceramics, in which sink-in predominates,[20] but one may expect errors when the method is applied to soft metals that exhibit extensive pile-up.[42]

A method of characterising materials for pile-up and the types in which it is important have been developed in detail by *Bolshakov et al.* using a finite element method.[43,44] From a purely mechanical viewpoint, the fundamental material parameters controlling elastic/plastic deformation during indentation are the elastic constants, E and ν, the yield stress, σ_y, and the work-hardening rate, η. However, a convenient, experimentally measurable parameter can be used to identify the expected indentation behaviour of a given material. The parameter is the ratio of the final indentation depth to the displacement at peak load, h_f/h_{max}, which is independent of the indenter penetration due to the self-similar geometry of the conical indenter.

The pile-up or sink-in behaviour depends on the amount of work hardening as well as on the value of h_f/h_{max}. These observations are shown in figure 2.6, which illustrate the surface profiles of two different types of materials considered in the finite element simulations. Specifically, the pile-up is large only when $h_f/h_{max} \approx 1$ and the amount of work hardening is small. Nevertheless, when $h_f/h_{max} < 0.7$, very little pile-up is present, irrespectively of the work hardening behaviour of the material.

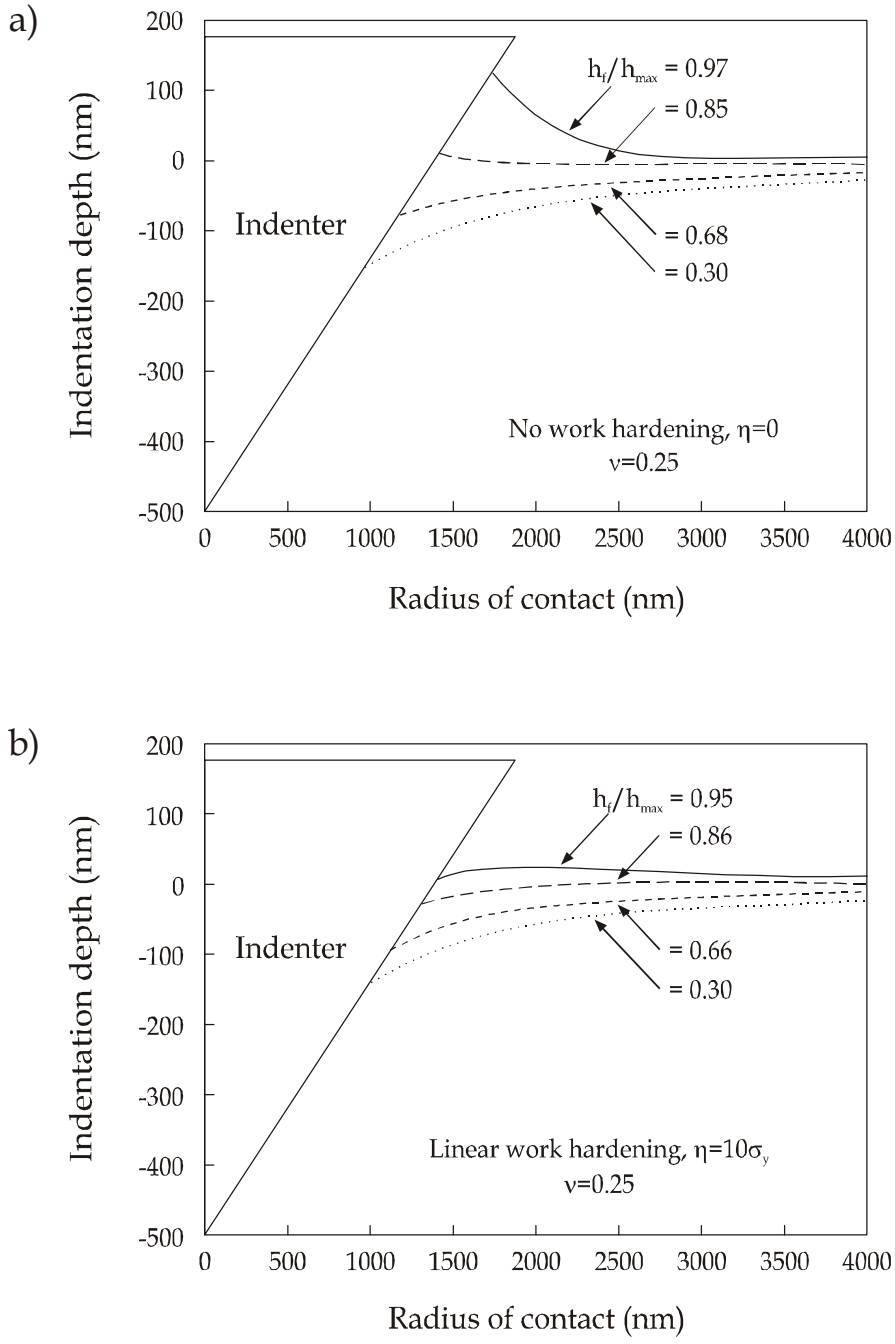

Figure 2.6 *Indentation contact profiles of elastic/plastic material calculated using a finite element code. Two separate cases of work hardening rate, ($\eta=d\sigma/d\varepsilon$), were considered:* (a) *elastic perfectly-plastic behaviour ($\eta=0$);* (b) *elastic-work hardening plastic behaviour ($\eta=10\sigma_y$). The yield stress was varied between $\sigma_y=0.114$ and $\sigma_y=26.62$ GPa to examine different plastic responses, after Bolshakov.*[44]

The *Oliver* and *Pharr* method is based on an elastic analysis, which can account for sink-in only. Therefore, the accuracy of the method in estimating the real contact area depends on the amount of pile-up. Furthermore, when $h_f/h_{max} > 0.7$, the accuracy of the method relies strongly on the work-hardening characteristic of the material. If the material does not work harden, the method underestimates the contact areas by as much as 60%. On the other hand, the contact areas for materials with a large amount of work hardening are predicted very well by the method. At this point it should be noted that from an experimental point of view, it is not possible to predict whether a material work-hardens solely based on load-displacement data. Conversely, when the pile-up is small i.e., $h_f/h_{max} < 0.7$, the method gives a good estimate of the contact area, independent of the work hardening behaviour. As hardness values are obtained for a given material using Eq. (2.7), inaccuracies in the contact area caused by not accounting for pile-up leads to similar inaccuracies in the hardness.

Similarly, according to Eq. (2.9), the reduced modulus is also overestimated when pile-up is important (i.e., the overestimation is great as ~50% when $h_f/h_{max} \approx 1$). Curiously, the finite element calculations show that even when pile-up is negligible, that is, materials with high yield stresses and/or high work hardening, the reduced modulus is still overestimated by 2-9%. Altogether, when measuring mechanical properties by nanoindentation, care must be taken when $h_f/h_{max} > 0.7$, since the use of the *Oliver* and *Pharr* method can lead to large errors in the contact area, and consequently, in the hardness and elastic modulus.

The problem of overestimation of the elastic modulus was addressed by *Hay et. al.*[45] It was established that the *Sneddon's* solution used for the analysis of indentation load-displacement data does not adequately describe the contact by a rigid cone, because the boundary conditions result in a cusp-shaped deformation within the contact radius rather than the prescribed conical shape. Therefore, a correction factor is needed to account for radial displacements and Eq. (2.6) should be rewritten as

$$S = \frac{2}{\sqrt{\pi}} \beta E_r \gamma \sqrt{A} \tag{2.14}$$

where γ is the correction factor, which depends on the Poisson's ratio of the material and the half angle of the indenter, ϕ. Analytical approximations for γ derived by applying simple modifications to *Sneddon's* solution and taken into account that a conical indenter with a semi-vertical angle of $\phi = 70.32^{o}$ gives the same area to depth ratio as the Berkovich indenter, yields

$$\gamma = \pi \frac{\pi/4 + 0.15483073 \cot\phi \dfrac{(1-2\nu)}{4(1-\nu)}}{\left(\pi/2 - 0.83119312 \cot\phi \dfrac{(1-2\nu)}{4(1-\nu)}\right)^2} \qquad (2.15)$$

When the procedure for the correction of the *Sneddon's* solution is applied, the hardness obtained by the *Oliver* and *Pharr* method, is underestimated by about 16.5%. The applicability of the correction factor to estimate the deviation on the effective Young's modulus is not straightforward as in the case of the hardness. However, for a material with $\nu = 0.25$, the correction reduces the effective modulus by about 7.4%. Thus, when the method is applied to materials that do not exhibit pile-up, there is an explanation for the overestimation of the modulus observed in the finite element results.

MATERIAL'S "FINGERPRINT"

The continuously sensed load and displacement provide a mechanical fingerprint[46] of a material response to deformation. Thus, traditional mechanical properties parameters such as the Young's modulus and hardness can be calculated. These parameters are the ones commonly used for comparing the mechanical performance of materials, for assessing the behaviour of new materials, and for modelling the predicted deformation behaviour of coated systems. However, a range of other parameters can be calculated from the nanoindentation curve which allows deformation responses to be both quantified and compared. These parameters, illustrated in figure 2.5, include:

(i) h_{max}, total surface deflection for a given peak load;
(ii) h_f, residual displacement after unloading, obtained after elastic recovery of the surface flexure. It provides a measure of the plastic component of the surface response;
(iii) W, hysteresis loop energy, defined as the energy enclosed with the indentation loading-unloading paths, which is the irreversible energy consumption associated with the plastic deformation;
(iv) S, contact stiffness for a given displacement, obtained through Eq. (2.10);
(v) $\%R$, proportion of the loaded displacement recoverable during unloading (0% = fully plastic contact response; 100% = fully elastic contact response);
(vi) H_L, hardness value calculated from maximum displacement, which includes the elastic and plastic contributions to the overall deformation;
(vii) H_R, conventional hardness value obtained from the residual displacement, it reflects only plastic component of deformation;

The use of nanoindentation for exploration of the properties of coated systems provides additional qualitative and quantitative insights into the response behaviour. For example, through careful comparison of the load-displacement curves for the coated system with those of the substrate alone, it is possible to assess the changes conferred by the coating on the maximum indenter displacement at a given contact load, the elastic and plastic works of indentation, and the amount of elastic recovery on unloading. Further, the transition from coating to substrate dominance with increasing applied load can be ascertained by changes in the detailed shapes and slopes of the loading curves. Moreover, the presence of displacement discontinuities "pop-ins" on loading curves may indicate defect nucleation in either the coating or the substrate (i.e. an elastic-plastic transition) or the nucleation of through-thickness cracks in the coating (i.e. the onset of coating fracture). Finally, the slope of the upper portion of the unloading curve, which is related to the contact elastic modulus (see Eq. (2.6)), gives an indication whether the elastic recovery of the indentation depth is dominated by the coating (which, therefore, still support the load) or the substrate (showing that the coating has cracked sufficiently to be non-load-bearing).

ANALYSIS OF NANOINDENTATION LOADING CURVES

As mentioned above, the attractive feature of nanoindentation is that the load-displacement curve provides information of the hardness, Young's modulus, and amount of work of indentation. Generally, these parameters are quantified by means of analysing the unloading curve. These approaches were originally applied for bulk homogeneous materials such as fused silica, tungsten, and aluminium. However, for composite materials like coated systems is not always possible to determine mechanical property data from the unloading curves. If the unloading segment is highly curved neither of these models are particularly appropriate for an estimate of the real contact area and thus mechanical properties of the material.

An alternative approach, in these situations, is to understand the shape of the loading curve in terms of the relationship between elastic modulus, hardness, indenter geometry, and the resultant maximum displacement for a given load. Moreover, an ongoing issue is whether or not coating properties can ever be quantified by sufficiently shallow nanoindentation and, if so, how the experimental conditions for such measurements might be identified. A recently proposed method to analyse the mechanical properties of the system by means of the loading curve, is based on the overall response of the material to the applied load, being modelled as the sum of its elastic and plastic components.[47] Thus, if the material being indented is rigid plastic, the contact radius, a, can be expressed as

$$a = \sqrt{\frac{P}{H}} \tag{2.16}$$

where P is the load and H the hardness (which is assumed constant with decreasing load). For conical and pyramidal indenters, the plastic depth of indentations, δ_p, is directly related to the characteristic radius of contact by

$$\delta_p = \phi a \tag{2.17}$$

where, ϕ, is a constant which is dependent on the cross-section and the angle of the particular indenter. This leads to

$$\delta_p = \phi\sqrt{\frac{P}{H}} \tag{2.18}$$

In addition, for real materials, there is a further instantaneous elastic contribution, δ_e, which, by dimensional analysis, has the form

$$\delta_e = \psi\frac{P}{Ea} \tag{2.19}$$

where E is the Young's modulus and ψ is another empirical constant. Substituting from Eq. (2.16) for a and summing the elastic and plastic contributions to δ, gives

$$P = E\left(\psi\sqrt{\frac{H}{E}} + \phi\sqrt{\frac{E}{H}}\right)^{-2}\delta^2 \tag{2.20}$$

Eq.(2.20) can be written in the form $P = K_m\delta^2$. The geometrical constants ψ and ϕ were experimentally determined to have the values ψ=0.5233 and ϕ=0.2177 for the Berkovich indenter used in this thesis. Thus, the constant K_m can be readily calculated for a material if E and H are known. As shown in figure 2.7, plots of $P-\delta^2$ produces good linear fits for a wide range of homogeneous materials chosen to exhibit a significant variety of E and H values. However, it should be noted, that at small displacements (i.e., δ < 20 nm), distinct changes in the shape of the $P-\delta^2$ can be seen. This scale is commensurate not only with the range at which elastic-only deformation may occur but also with the dimension of the indenter end-region where geometrical self similarity is not expected to hold because of its finite radius of curvature. Therefore, away from the area close to the origin, each of these plots can be fitted to a straight line whose gradient gives a value for K_{exp} (from here on referred as the experimentally determined constant).

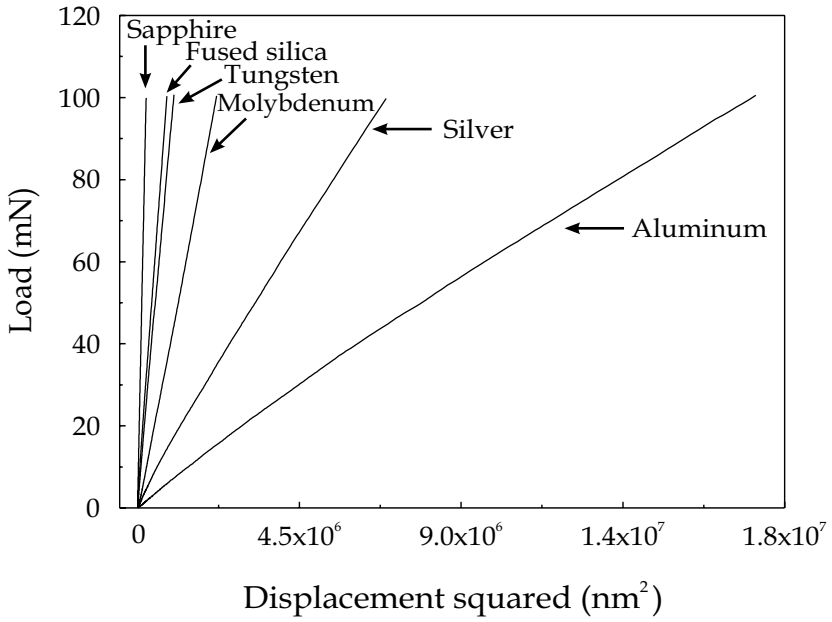

Figure 2.7 *Wide range of displacement squared values resulting from the same maximum applied load, 100 mN. The experimental nanoindentation loading curves were recorded for six homogeneous materials constituing a broad combination of E and H values. Note the linear P- ^{2} relationship from where a best fit value of K_{exp} can be measured.*

The proximity of the resulting equality between K_m and K_{exp} for the homogeneous materials depicted in figure 2.7 can be judged by inspecting figure 2.8. It is clear that a very good fit to the loading curves for a wide range of materials can be obtained using Eq. (2.20) with ψ=0.5233 and ϕ=0.2177. Further, given K_{exp}, it is possible to calculate values of E and H, though one has to be known in order for the other to be calculated explicitly.

The load-displacement squared curve can also be used to describe the response of coated systems where, with increasing indenter displacement, the elasto-plastic behaviour of the system is expected to change from a coating - dominated regime to a substrate - dominated regime. Therefore, initially, the indenter should just probe merely the properties of the coating. The expected dependence is simply a straight line. The slope would be that predicted from the above expression for K_m by inserting the Young's modulus and hardness

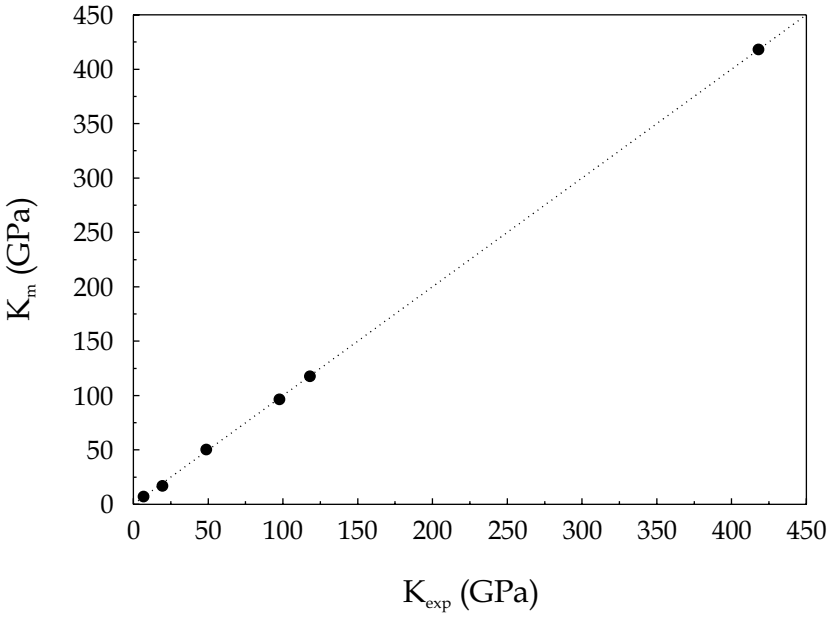

Figure 2.8 *High consistency of the correlation between K_{exp} (experimentally determined constant in the P- ^{2} relationship) and K_m (determined from Eq.(2.20)).*

values for the coating. Subsequently, there should be a transition region where the slope of the curve is more complex as the coating, the interfacial region, and the substrate all deform together. In this region, the relationship $P-\delta^2$ will not necessarily display either the same slope or even be a straight line. Finally, at large displacements, the highly-fractured coating will no longer play any significant rule in supporting the applied load and the predicted curve should again be a straight line with a slope that can be predicted from the Young's modulus and hardness of the substrate.[48]

The model is used throughout this thesis, not only to measure the coating Young's modulus and hardness values, but also to provide a tractable experimental approach to determine the range of loads and displacements over which the coating is found to dominate the system behaviour. Within this range, the coating properties can be measured (thus removing the reliance on empirical rules such as the less than 10% of coating thickness). An important practical problem regarding the measurement of the coating hardness values in systems with either very hard coatings or soft substrates, is to ensure that at this

very small indenter displacements it is in fact only the coating that is plastically deformed. The necessary requirement is that the maximum Hertz shear stress generated by the indenter (which is at a small depth below the surface) should lie in the coating and it also should exceed the yield stress before substrate is plastically yielding.[49]

NANOINDENTER INSTRUMENTS

Ultra low load indentation (nanoindentation) experiments were carried out at room temperature and ambient atmosphere using both a home-built at Technical University of Eindhoven apparatus and a MTS Nano Indenter® XP. The home-built nanoindenter consists of a force and displacement measurement units and an *xy* table. A Berkovich diamond tip is attached to a coil-magnet assembly, and suspended on leaf springs. Suppressing any vertical movement of this assembly during indentation (using a PID controlled inductive displacement sensor above it) yields an accurate and easily calibrated force measurement with a range from 1 mN to 1 N and with an accuracy of roughly 0.025%. The instrument operates in a displacement-controlled mode, where indentation is achieved by moving the specimen towards the indenter, with a second coil magnet assembly, also suspended on leaf springs. The displacement is derived from the signal of three inductive transducers symmetrically surrounding the indenter. Displacements anywhere between 0 and 250 micrometer can be measured with an accuracy of about 1 nm. Measured displacements are fed to a feedback loop that governs the indentation movement.

The Nano Indenter® XP can be operated in both displacement-controlled and load-controlled mode. In this case, the Berkovich indenter which is driven toward the specimen by mean of a coil and magnet assembly located at the top of the loading column. The force imposed on the indenter is controlled by varying the current in the coil and the position determined by a capacitance displacement gauge. The loading column is suspended by flexible springs and the motion is damped by airflow around the centre plate of the capacitor, which is attached to the loading column. The capacitance displacement gauge allows

one to detect displacement changes of 0.04 nm, and the force resolution of the system is about 75 nN.

One of the advantages of the Nano Indenter® XP over the home-built indenter is being equipped with the continuous stiffness measurement (CSM) option. This technique enables the contact stiffness to be measured continuously during the loading portion of the test, thereby differing from the conventional load-displacement-time method where only one contact stiffness measurement is made from the unloading portion of the experiment at P_{max}. The continuous contact stiffness measurement is accomplished by superimposing a small sinusoidal oscillation on the primary loading signal. The amplitude of the force oscillation is controlled in such a way that the displacement oscillation remained constant at 1 nm. The indentation system and contact together are modelled as a simple harmonic oscillator. Thus, by monitoring the ratio between force and displacement oscillation amplitudes, as well as the phase shift between the two, the elastic stiffness of the contact may be inferred continuously as the indenter penetrates the material.[20] The data extracted is used to provide a continuous measurement of the hardness and elastic modulus as a function of either depth or applied load.

A typical load-unload cycle consists of approaching the indenter tip to the specimen at a rate of 10 nm/s until the surface contact is detected by a change in contact stiffness. The indenter is then driven into the sample at a constant loading rate *(dP/P)* of 0.05, allowing large numbers of date points to be accumulated in the low-load segment. At peak load, the indenter is hold for 10 s to allow any time-dependent plasticity, creep, to take place. Then, the sample is unload until 70% of the peak value where a hold period of 100 s is performed to compensate for any thermal drift in the data. This is done by assuming the drift rate was constant during the test. After the drift correction, the indenter is removed from the sample.

2.4.3 ROLLING CONTACT FATIGUE

Rolling contact fatigue (RCF) experiments were performed to study the resistance of PVD coated tool steel against surface fatigue. This type of failure is

often manifested by the formation of spalling or pitting on rolling surfaces. Contact between the test sample and the counterpart material is non-conforming and when they are loaded together the surface of contact is elliptical in shape.[50] In a pure rolling contact situation, the maximum compressive stress exists at the surface in the centre of the contact and the maximum shear stress perpendicular to the surface is developed beneath the contact region. The depth depends upon the applied load, the elastic properties of the two contacting bodies and the coating thickness.[51] The stress distribution is illustrated in figure 2.9. The Huber-von Mises yield criterion, predicting that plastic flow occurs when the equivalent stress is equal to the yield strength, is the critical factor in defining the wear mechanism in rolling contact. It describes the stress at which the onset of plastic deformation is expected ultimately causing adhesive failure and delamination. Therefore, the equivalent stress had to be calculated for each combination of coated system/counterpart material to

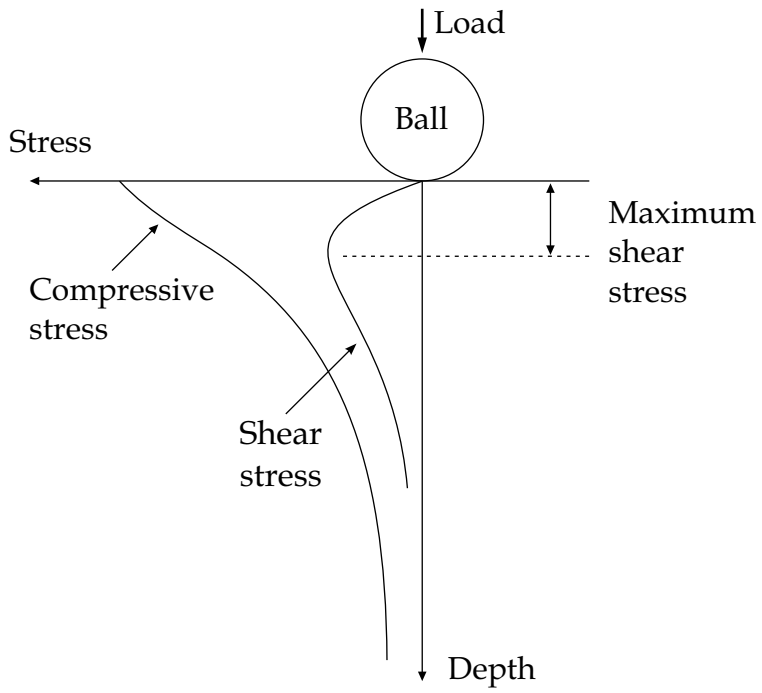

Figure 2.9 *Schematic illustration of stress distribution at a typical point contact.*

establish the maximum contact pressure when the elastic-plastic regime commences. After calculating this value, the experiments could be designed for an initial elastic deformation condition bearing out that the only fracture process was fatigue failure. The equivalent stress was calculated using the *El-Sherbiney* and *Halling's* theory[52] for elastic deformation. The rolling contact fatigue experiments were carried out in a modified pin-on-ring tester, schematically depicted in figure 2.10. All tests were performed under mineral oil (BP Energol CS 68) lubricated conditions. The oil acts as a coolant keeping the temperature at a level between 20 °C and 30 °C. Contact was achieved by pressing a ball, made of commercially available tungsten carbide with a radius of curvature, R=8.0 mm, against the outer diameter of the ring under a known normal load, F_N. The ball rotated in a bronze socket along a fixed axis parallel to the axis of rotation of the ring, resulting in a pure rolling contact of ball and ring.

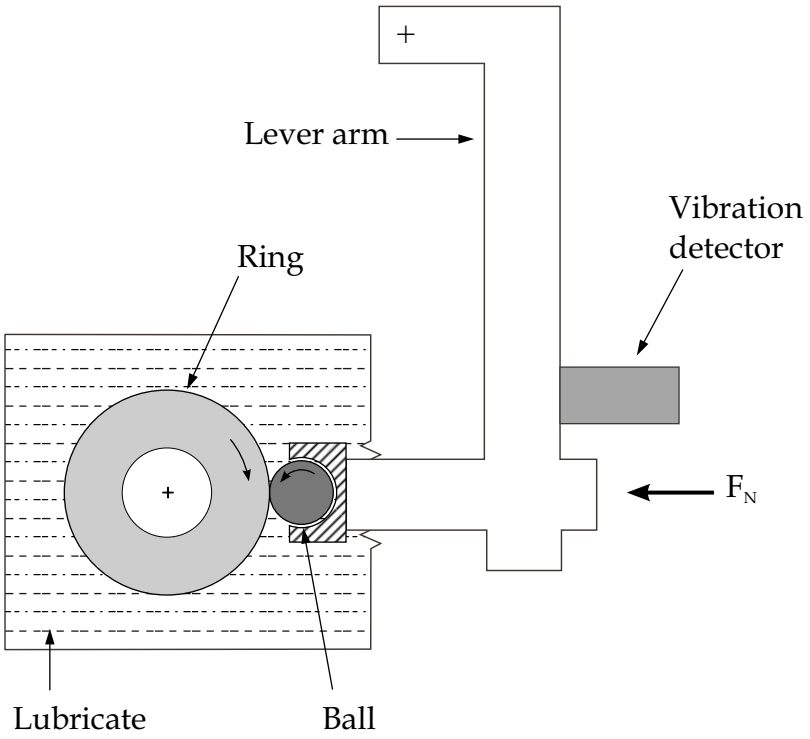

Figure 2.10 *Schematic of the rolling ball on ring equipment (modified pin-on-ring tester).*

The rings have a radius of curvature, R=30.0 mm, and a width of 13 mm, and were rotated at a speed of 500 revolutions per minute, corresponding to a contact speed of 1.6 $m.s^{-1}$.

A vibration detector was mounted on the lever arm to detect the surface deterioration as a result of surface fatigue. The fatigue lifetime was reached when 1% of the contact path on the ring outer diameter showed delamination by visual inspection. The increase in vibration level corresponding to 1% delamination was found to be in the range of 15% to 20%. Therefore, the tests stopped automatically when the selected vibration level was reached. As tungsten carbide has a very high resistance against surface fatigue, the ball will usually survive many tests. Still as a rule, for each test a new ball was used. By shifting the ring in the axial direction, it was possible to perform about five tests per ring.

References

1. D.S. Rickerby, S.J. Bull, Surf. Coatings Technol. **39-40**, 315 (1989).
2. O. Knotek, F. Löffler, G. Krämer, Surf. Coatings Technol. **59**, 14 (1993).
3. K. Holmberg, A. Matthews, *Coatings Tribology*, D. Dowson (Ed.), Tribology series 28, Elsevier, Amsterdam, (1994).
4. S. Kadlec, J. Musil, W.-D. Münz, G. Håkanson, J.-E. Sundgren, Surf. Coatings Technol. **39-40**, 487 (1989).
5. H. Randhawa, P.C. Johnson, Surf. Coatings Technol. **31**, 303 (1987).
6. L.R. Boxman, S. Goldsmith, Surf. Coatings Technol. **52**, 39 (1992).
7. B.D. Cullity, *Elements of X-ray Diffraction*, addisonn-Wesley, MA, (1978).
8. H.E. Cheng, M.H. Hon, J. Appl. Phys. **79**, 8047 (1996).
9. M. Prutton, L.A. Larson, H. Poppa, J. Appl. Phys. **54**, 374 (1983).
10. S.B. Newcomb, C.B. Boothroyd, W.M. Stobbs, Journal of Microscopy **140**, 195 (1985).
11. G. Radnóczi, Á. Barna, Surf. Coatings Technol. **80**, 89 (1996).
12. G.F. Voort, G.M. Lucas, Advanced Materials & Processes **9**, 21 (1998).
13. H. Bückle, in *The Science of Hardness Testing and its Research Applications*, J.W. Westbrook, H. Conrad (Eds.), American Society for Metals, Metals Park, Ohio, (1973).
14. B. Jönsson, S. Hogmark, Thin Solid Films **114**, 257 (1984).
15. J.P. Burnett, D.S. Rickerby, Thin Solid Films **148**, 41 (1987).

16. D. Chicot, J. Lesage, Thin Solid Films **254**, 123 (1995).
17. J.B. Pethica, R. Hutchings, W.C. Oliver, Phil. Mag. A **48**, 593 (1983).
18. D. Stone, W.R. LaFontaine, P. Alexopoulos, T.-W. Wu, C.Y. Li, J. Mater. Res. **3**, 141 (1988).
19. J.S. Field, M.V.Swain, J. Mater. Res. **8**, 297 (1993).
20. W.C. Oliver, G.M. Pharr, J. Mater. Res. **7**, 1564 (1992).
21. J.-L. Loubet, B.N. Lucas, W.C. Oliver, Mat. Res. Soc. Symp. Proc. **436,** 233 (1996).
22. M.J. Mayo, W.D. Nix, Acta Metall. **35**, 2183 (1988).
23. C.B. Ponton, R.D. Rawlings, Mater. Sci. Technol. **5**, 865 (1989).
24. M.V. Swain, J.T. Hagen, J.E. Field, J. Mater. Sci. **12**, 1914 (1977).
25. A. Niederhofer, P. Nesladek, S. Veprěk, Surf. Coatings Technol. **120-121**, 173 (1999).
26. E.R. Weppelmann, X.-Z. Hu, M.V. Swain, J. Adhesion Sci. Technol. **8**, 611 (1994).
27. W.W. Gerberich, D.E. Kramer, N.I. Tymiak, Acta Mater. **47**, 4115 (1999).
28. D. Tabor, in *Microindentation Techniques in Materials Science and Engineering*, P.J. Blau, B.R. Lawn (Eds.), American Society for testing and Materials, Philadelphia, (1986).
29. J.L. Hay, M.E. O'Hern, W.C. Oliver, Mat. Res. Soc. Symp. Proc. **522**, 27 (1998).
30. N.A. Stillwell, D. Tabor, Proc. Phys. Soc. London **78**, 169 (1961).
31. J.-L. Loubet, J.M. Georges, O. Marchesini, G. Meille, J. Tribology **106**, 43 (1984).
32. M.F. Doerner, W.D. Nix, J. Mater. Res. **1**, 601 (1986).
33. G.M. Pharr, W.C. Oliver, F.R. Brotzen, J. Mater. Res. **7**, 613 (1992).
34. J. Boussinesq, *Applications des Potentiels a l'étude de équilibre et du mouvement des solides élastiques*, Gauthier-Villars, Paris, (1885).
35. H. Hertz, J. reine und angewandte Mathematik **92**, 156 (1882).
36. A.E.H. Love, Philos. Trans. A **228**, 377 (1929).
37. A.E.H. Love, Quart. J. Math. **10**, 161 (1939).
38. J.W. Harding, I.N. Sneddon, Proc. Cambridge Philos. Soc. **41**, 16 (1945).
39. S.I. Bulychev, V.P. Alekhin, M.Kh. Shorshorov, A.P. Ternovskii, G.D. Shnyrev, Zavod. Lab. **41**, 1137 (1975).
40. I.N. Sneddon, Int. J. Engng. Sci. **3**, 47 (1965).
41. R.B. King, Int. J. Solids Structures **23**, 1657 (1987).
42. A. Bolshakov, W.C. Oliver, G.M. Pharr, J. Mater. Res. **11**, 760 (1996).
43. A. Bolshakov, W.C. Oliver, G.M. Pharr, Mat. Res. Soc. Symp. Proc. **436**, 141 (1997).
44. A. Bolshakov, G.M. Pharr, J. Mater. Res. **13**, 1049 (1998).
45. J.C. Hay, A. Bolshakov, G.M. Pharr, J. Mater. Res. **14**, 2296 (1999).
46. T.F. Page, S. V. Hainsworth, Surf. Coatings Technol. **68-69**, 571 (1994).
47. S.V. Hainsworth, H.W. Chandler, T.F. Page, J. Mater. Res. **11**, 1987 (1996).
48. S.V. Hainsworth, M.R. McGurk, T.F. Page, Surf. Coatings Technol. **102**, 97 (1998).

49. S.V. Hainsworth, T.F. Page, Mat. Res. Soc. Symp. Proc. **436**, 171 (1997).
50. K.L. Johnson, *Contact Mechanics*, Cambridge University Press, (1985).
51. K. Mao, Y. Sun, T Bell, Surface Engineering **10**, 297 (1994).
52. M.G.D. El-Sherbiney, J. Halling, Wear **40**, 325 (1976).